Article
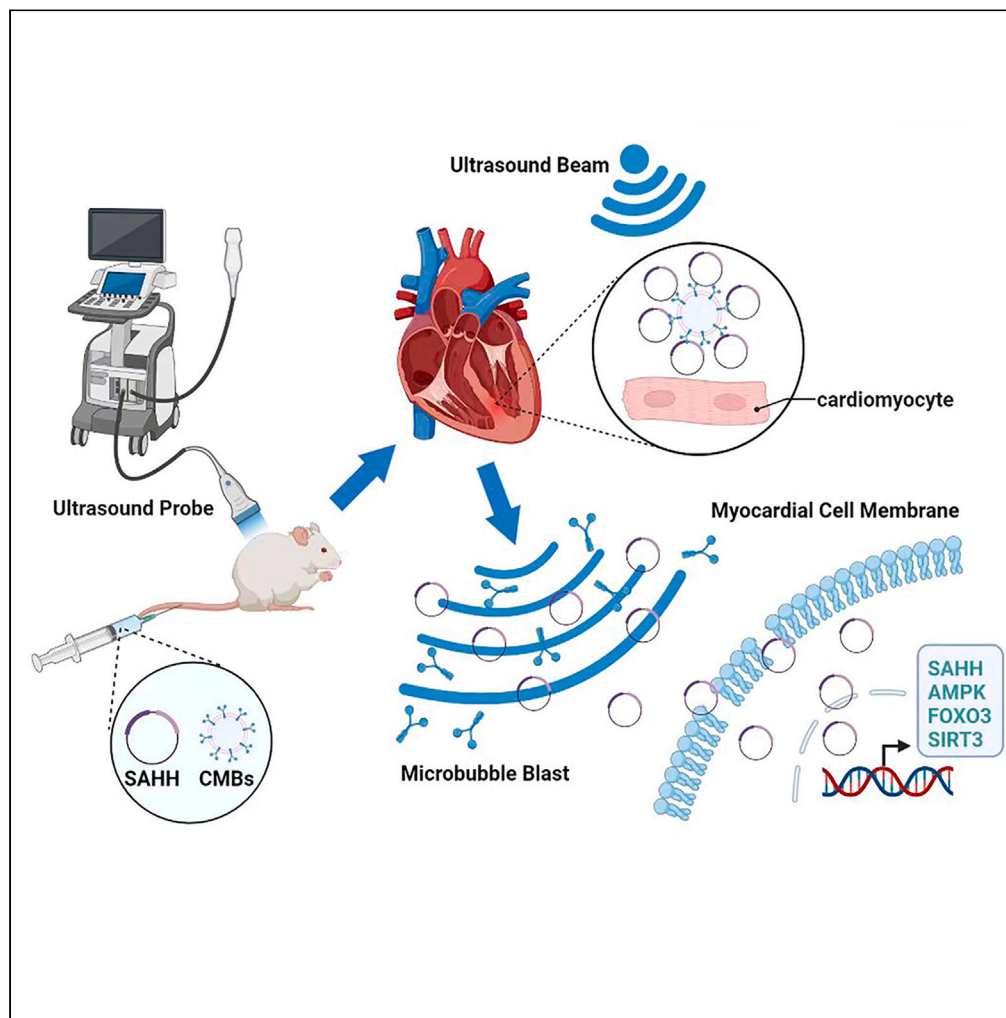
Ultrasound-targeted microbubble technology facilitates SAHH gene delivery to treat diabetic cardiomyopathy by activating AMPK pathway

Xiaohui Guo, Kegong Chen, Lin Ji, Shanjie Wang, Xiangmei Ye, Liang Xu, Leiguang Feng

leiguangfeng@163.com

Highlights

The mixture of CMBs and SAHH plasmid were transported toward the heart of rats

SAHH-loaded CMBs can be destroyed to release the plasmid after reaching the heart

The SAHH-containing plasmid then induced the expression of AMPK/FOXO3/SIRT3 pathway

The SAHH-containing plasmid/CMBs improved cardiac function

Article

Ultrasound-targeted microbubble technology facilitates SAHH gene delivery to treat diabetic cardiomyopathy by activating AMPK pathway

Xiaohui Guo,[1,2,6] Kegong Chen,[3,6] Lin Ji,[4] Shanjie Wang,[2] Xiangmei Ye,[1] Liang Xu,[5] and Leiguang Feng[1,7,*]

SUMMARY

Diabetic cardiomyopathy (DCM) is a cardiovascular complication with no known cure. In this study, we evaluated the combination of ultrasound-targeted microbubble destruction (UTMD) and cationic microbubbles (CMBs) for cardiac S-adenosyl homocysteine hydrolase (SAHH) gene transfection as potential DCM therapy. Models of high glucose/fat (HG/HF)-induced H9C2 cells and streptozotocin-induced DCM rats were established. Ultrasound-mediated *SAHH* delivery using CMBs was a safe and noninvasive approach for spatially localized drug administration both *in vitro* and *in vivo*. Notably, *SAHH* overexpression increased cell viability and antioxidative stress and inhibited apoptosis of HG/HF-induced H9C2 cells. Likewise, UTMD-mediated *SAHH* delivery attenuated apoptosis, oxidative stress, cardiac fibrosis, and myocardial dysfunction in DCM rats. Activation of the AMPK/FOXO3/SIRT3 signaling pathway may be a key mechanism mediating the role of SAHH in regulating myocardial injury. Thus, UTMD-mediated *SAHH* transfection may be an important advancement in cardiac gene therapy for restoring ventricular function after DCM.

INTRODUCTION

Type 2 diabetes is a severe and common chronic disease caused by complex genetic and environmental factors. Diabetes and its complications are major global public health issues that affect people in both developed and developing countries.[1] In patients with diabetes, the risk of developing heart failure is five times greater than that in nondiabetic patients, indicating poor prognosis.[2] Despite recent advancements in clinical and basic research on diabetic cardiomyopathy (DCM) or diabetes-related heart failure over the past decade, the mechanism underlying its pathogenesis remains elusive, and a consensus on prevention and treatment methods has not been reached.[2] Therefore, it is important to elucidate the molecular mechanisms underlying DCM to develop more effective therapies.

S-Adenosylhomocysteine (SAH) is the precursor of homocysteine, the reversible hydrolysis of which to adenosine and L-homocysteine is catalyzed by SAH hydrolase (SAHH).[3] Increased plasma levels of SAH have been associated with the risk of cardiovascular diseases in humans.[4,5] Xiao et al.[6] showed that SAHH inhibition resulted in increased plasma levels of SAH and induced endothelial dysfunction via oxidative stress. Likewise, adenosine dialdehyde (ADA) inhibited SAHH, increased intracellular or plasma levels of SAH, aggravated high glucose-induced podocyte injury, and exacerbated nephropathy in a mouse model of STZ-induced diabetes. Dai et al.[7] also observed that inhibition of SAHH in heterozygous *SAHH*-knockout mice aggravated inflammation, oxidative stress, and diabetic nephropathy. Endothelial cell senescence plays an important role in the development of atherosclerosis. Inhibition of SAHH can induce endothelial cell senescence by downregulating the expression of human telomerase reverse transcriptase (hTERT), whereas overexpression of hTERT can rescue SAHH inhibition-induced endothelial cell senescence.[8] Inhibition or deficiency of SAHH can lead to a decrease in the AdoMet/AdoHcy ratio, resulting in demethylation damage. Overexpression of SAHH by 2–10 times led to a decrease in the levels of intracellular AdoHcy and an increase in those of adenosine.[9] Therefore, we hypothesized that SAHH overexpression could alleviate HG/HF-induced oxidative stress injury in H9C2 cells and improve cardiac function in DCM rats.

Gene therapy improves cardiac remodeling and promotes the recovery of ventricular function in patients with cardiomyopathy; however, the low gene editing efficiency of target organs severely affects treatment potential.[10] Ultrasound-targeted microbubble destruction (UTMD) is a novel gene-targeting delivery system that provides minimally invasive, repeatable, and targeted gene delivery to injured myocardial tissue, improving cardiac function.[11,12] Clinical trials have shown that ultrasound microbubbles are safe for thrombolytic therapy and

[1]Department of Clinical Laboratory, First Affiliated Hospital of Harbin Medical University, Harbin 150081, P.R. China
[2]The Key Laboratory of Myocardial Ischemia, Chinese Ministry of Education, Harbin 150086, P.R. China
[3]Department of Thoracic Surgery, First Affiliated Hospital of Anhui Medical University, Hefei 230022, P.R. China
[4]Department of Orthopedics, The First Hospital of Harbin, Harbin 150010, P.R. China
[5]Department of Cardiology, The Second Hospital of Harbin, Harbin 150056, P.R. China
[6]These authors contributed equally
[7]Lead contact
*Correspondence: leiguangfeng@163.com
https://doi.org/10.1016/j.isci.2024.108852

tumor adjuvant chemotherapy.[13,14] In our previous study, we developed a positively charged carrier called cationic microbubbles (CMBs), the binding ability of which was enhanced by the incorporation of the melatonin receptor RORα. After mixing RORα with CMBs *in vitro* and intravenously injecting them into small animals using ultrasound for organ targeting and microbubble destruction, a local cavitation effect was produced, which increased gene expression in the targeted organ and optimized the therapeutic effect of melatonin on septic cardiomyopathy.[15]

In the present study, we constructed a UTMD gene delivery system for the transfection of SAHH plasmids to the heart. We used octafluoropropane (C3F8) as the core gas to synthesize CMBs with a strong carrying capacity for negative charges on SAHH plasmids. When the CMB complex and SAHH gene were exposed to low-intensity ultrasound, the microbubbles produced a cavitation effect, causing reversible pores on the membrane of myocardial cells. Subsequently, rupturing of the microbubbles released the SAHH gene, which entered into the cells through these pores. UTMD local burst technology was used to achieve targeted delivery of SAHH. To test whether targeted delivery of the SAHH gene could effectively prevent DCM, an HG/HF-induced H9C2 cell *in vitro* model and an STZ-induced type 2 diabetic rat *in vivo* model were established. We found that SAHH enhanced the antioxidant stress damage and antiapoptotic ability of H9C2 cells, reduced oxidative stress damage and fibrosis in rats with DCM, improved heart function, and reduced the apoptosis of myocardial cells. Therefore, ultrasound-targeted microbubble technology-mediated SAHH gene transfer can prevent diabetes-induced heart dysfunction and may serve as a new and effective future clinical treatment strategy for preventing DCM.

RESULTS

Expression of *SAHH* was decreased in rats with STZ-induced DCM and HG/HF-treated H9C2 cells

We first generated a DCM rat model induced by HG/HF feeding and low-dose STZ injection. We found that the mRNA expression of *SAHH* in the DCM group was reduced compared with that in the control group (Figure 1A). In addition, immunofluorescence and western blot analyses revealed that the expression of SAHH in the DCM group was significantly lower than that in the control group (Figures 1B and 1C). Consistent with this, we observed the decreased mRNA and protein expression of SAHH in H9C2 cells induced by HG/HF (Figures 1D–1F). Conversely, we found that the levels of SAHH-related metabolites, SAH and Hcy, and those of the oxidative stress factor MDA were significantly increased in H9C2 cells induced by HG/HF compared with those in control cells (Figure 1G).

### SAHH overexpression improved the protective effect on H9C2 cells induced by HG/HF *in vitro*

We observed that after transfection of H9C2 cells with si-SAHH (knockdown) and ov-SAHH (overexpression) plasmids, the protein expression of SAHH was decreased and increased, respectively (Figure 2A). We next performed CCK8 assays to assess the effect of knocking down or overexpressing *SAHH* on cell proliferation. We found that compared with the control (si-Ctrl and vector), si-SAHH significantly reduced cell viability, whereas ov-SAHH significantly increased cell viability (Figure 2B). We further explored the effects of SAHH on the levels of reactive oxygen species (ROS) in H9C2 cells using DHE (dihydroethidium) staining. We accordingly detected that the antioxidative stress capacity of *SAHH*-modified H9C2 cells was enhanced (Figure 2C). Mitochondrial dysfunction is the primary cause of oxidative stress. We found significantly reduced levels of mitochondrial membrane potential in the HG/HF group compared with those in the control group; however, ov-SAHH significantly increased the levels of mitochondrial membrane potential (Figure 2D). Consistently, the levels of SAHH-related metabolites, SAH and Hcy, and those of MDA were significantly decreased in the ov-SAHH group compared with those in the control groups (si-Ctrl and vector) (Figure 3A). Moreover, apoptosis was attenuated in cells overexpressing *SAHH* compared with that in the control (si-Ctrl and vector) (Figure 3B). H9C2 cells induced by HG/HF showed significantly increased levels of proapoptotic signals, such as BAX, cleaved caspase-9, and cleaved caspase-3, and decreased expression of the antiapoptotic marker Bcl-2; these changes were considerably attenuated by *SAHH* overexpression (Figure 3C). These results suggested that *SAHH* overexpression may increase cell viability and inhibit injury in cardiomyocytes exposed to HG/HF, which warrants further *in vivo* validation.

Preparation and characterization of SAHH plasmids/CMBs

Using a Zeta Sizer 2000 (Malvern, Worcestershire, UK), we found that the average size of synthesized CMBs was 1,822 $\pm$ 202.5 nm, and the zeta potential was +26.2 $\pm$ 3.2 mV (Figure 4A). Transmission electron microscopy revealed that CMBs exhibited a hollow spherical shape, with particle sizes ranging from 0.5 to 1.5 μm (Figure 4B). We did not observe any specific changes in the concentration, particle diameter, or zeta potential of CMBs after 4 h of storage at 25°C (Figure 4C). On incubating var10–80 μg plasmids with 5×10^8/CMBs, we observed that the maximum CBM binding capacity occurred when 40 μg DNA was added (Figure 4D). Fluorescent microscopy following PI (propidium iodide) staining revealed that the SAHH-containing plasmid was conjugated to the surface of CMBs, emitting red fluorescence (Figure 4E). We also performed flow cytometry to quantify the plasmid loading capability of CMBs and found that PI-labeled SAHH-loaded CMBs accounted for 59.2 $\pm$ 4.8% of total CMBs (Figure 4F).

Evaluation of gene transfection efficiency and safety in cells

We incubated the plasmids with microbubbles at 25°C for 15 min. First, we inverted the H9C2 cells to maximize their exposure to microbubbles, followed by UTMD-mediated transfer of the *SAHH*-containing plasmid. We assessed the delivery efficiency of the plasmid/CMB mixtures in H9C2 cells using western blotting and found that the protein levels of SAHH were higher in the SAHH+UTMD group than in the other groups (Figure 5A). We also used the TUNEL assay to assess the damage to H9C2 cells 3 days after transfection; however, we did not observe
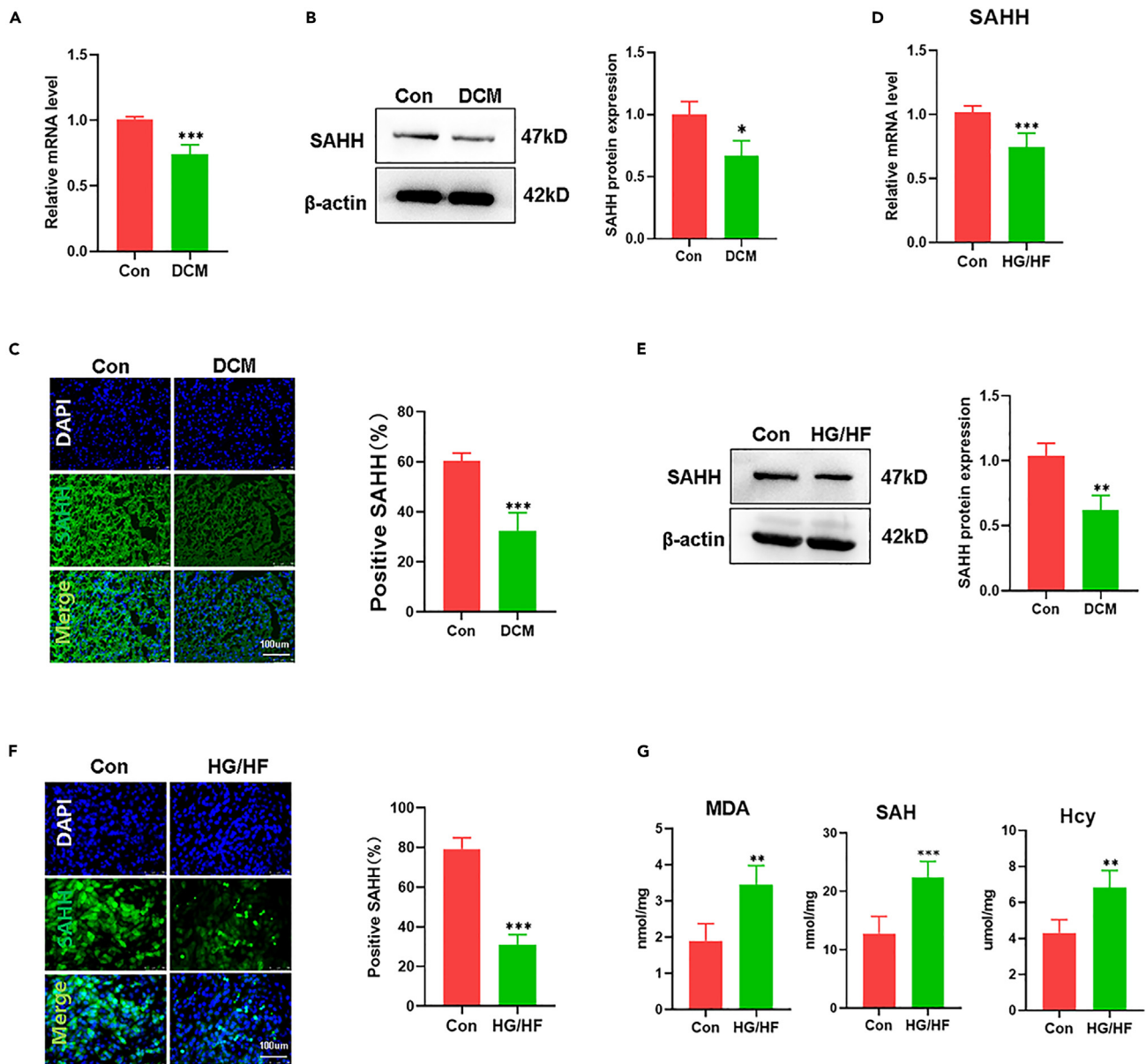
Figure 1. Comparing the changes in the expression of *SAHH* in both *in vivo* and *in vitro* models of diabetes

(A) Level of mRNA expression of SAHH in myocardial tissue (n = 5).

(B) Level of protein expression of SAHH in myocardial tissue (n = 5).

(C) SAHH expression was examined by immunofluorescence staining in myocardial tissues (scale bar: 100 μm).

(D) Level of mRNA expression of SAHH in H9C2 cells (n = 5).

(E) Level of protein expression of SAHH in H9C2 cells (n = 5).

(F) SAHH expression was examined by immunofluorescence staining in H9C2 cells (scale bar: 100 μm).

(G) Levels of the metabolites MDA (nmol/mg), SAH (nmol/mg), and Hcy (μmol/mg) in H9C2 cells (n = 5).

Data in bar plots are presented as mean ± SD. *p < 0.05; **p < 0.01; ***p < 0.001 versus Con group.

any obvious difference in the levels of apoptosis between groups (Figure 5B). We then harvested the supernatants and detected the LDH activity in different groups using ELISA. We determined that the LDH activity was not markedly different among groups (Figure 5C). We further used the expression of GFP (green fluorescent protein) to determine the efficiency of the UTMD-mediated transfer of the SAHH-GFP plasmid to H9C2 cells. We detected the GFP signal 72 h after transfection in cells using fluorescence microscopy. We found that the SAHH+UTMD group exhibited significantly higher levels of GFP expression than the other groups (Figure 5D). The transfection efficiency of the GFP plasmid in H9C2 cells using flow cytometry was found to be 27.09% (Figure 5E).
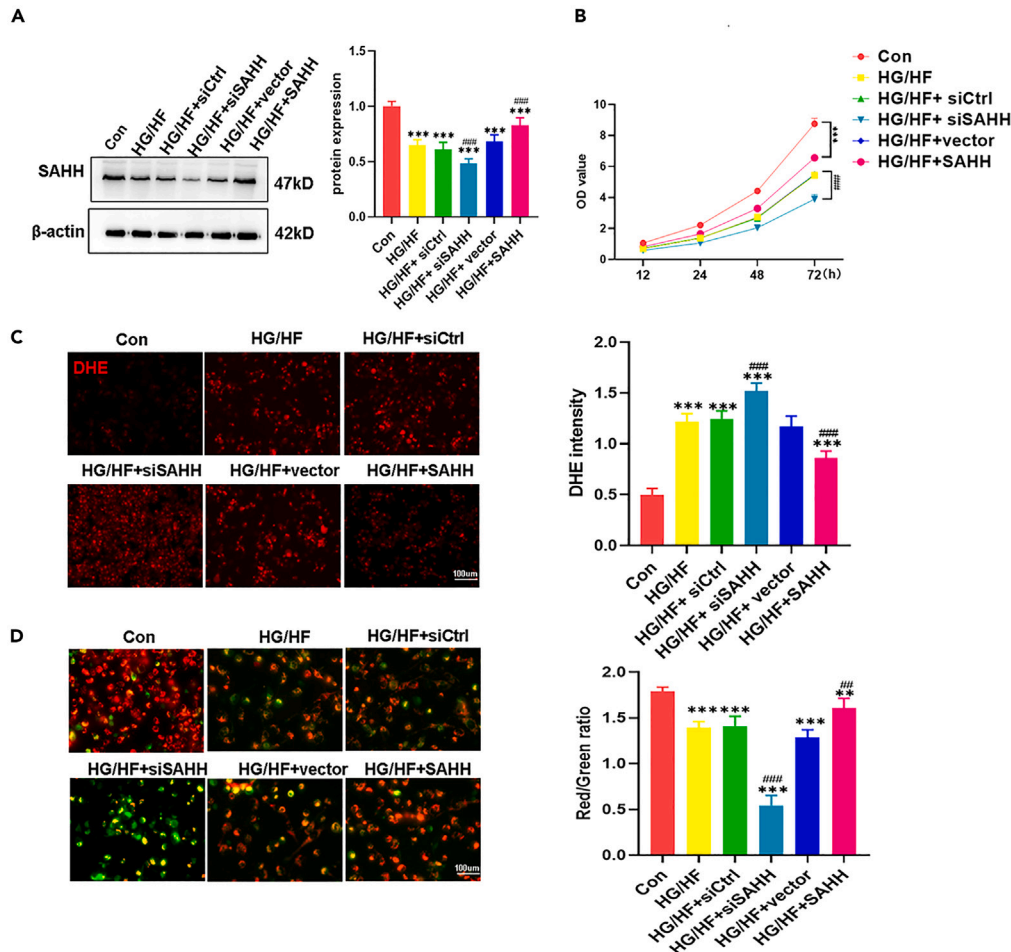
Figure 2. SAHH overexpression improved the proliferation and antioxidant status of HG/HF-induced cardiomyocytes *in vitro*

(A) Western blotting and quantification of the expression of SAHH in H9C2 cells transfected with si-SAHH or SAHH plasmid for 48 h (n = 4).

(B) Proliferation ability of H9C2 cells transfected with siSAHH or SAHH plasmid using MTT assay (n = 4).

(C) DHE immunofluorescence staining of H9C2 cells transfected with siSAHH or SAHH plasmid. DHE intensity was quantified to reflect the levels of ROS in H9C2 cells (n = 4, scale bar: 100 μm).

(D) JC-1 staining of H9C2 cells. The ratio of JC-1 aggregates (red) in healthy mitochondria and JC-1 monomers (green) in depolarized mitochondria was used to assess mitochondrial membrane potential (n = 4, scale bar: 100 μm).

Data in bar plots are presented as mean $\pm$ SD. **$p < 0.01$; ***$p < 0.001$ versus Con group, $^{\#\#}p < 0.01$; $^{\#\#\#}p < 0.001$ versus HG/HF group.

Efficiency of cardiac delivery of *SAHH*-containing plasmids via UTMD

First, we assessed the safety of UTMD for gene transfection. We evaluated the presence of CMBs in myocardial tissues and the release of plasmids from CMBs by ECG-triggered bursts using echocardiography (Figure 6A). Although ultrasound irradiation can produce cavitation effects, which may lead to possible pore reversibility, it did not cause injury to normal myocardial cells, as indicated by the insignificantly altered levels of plasma LDH and CK-MB (Figure 6B). We found that the protein levels of SAHH were not significantly different in the liver, spleen, lung, and kidney after UTMD; however, the level of SAHH in the heart tissue was significantly increased (Figure 6C). We detected the GFP signal in tissues 3 days after UTMD gene therapy (Figure 6D).

Effects of SAHH on cardiomyocyte apoptosis *in vivo*

We found that the expression of *SAHH* was increased in rats transfected with the ov-SAHH plasmid using UTMD (DM+ov-SAHH) compared with that in DCM groups (Figure 7A). We evaluated the protective effect of UTMD-mediated SAHH transfection on myocardial tissues one-month post-DCM using the TUNEL assay. We detected that the percentage of TUNEL-positive cardiomyocyte nuclei was significantly lower in ov-SAHH-treated hearts compared with that in DCM hearts (Figure 7B). Moreover, we noticed that the levels of proapoptotic signals, such as BAX, cleaved caspase-9, and cleaved caspase-3, were significantly increased, whereas the expression of the antiapoptotic Bcl-2 was
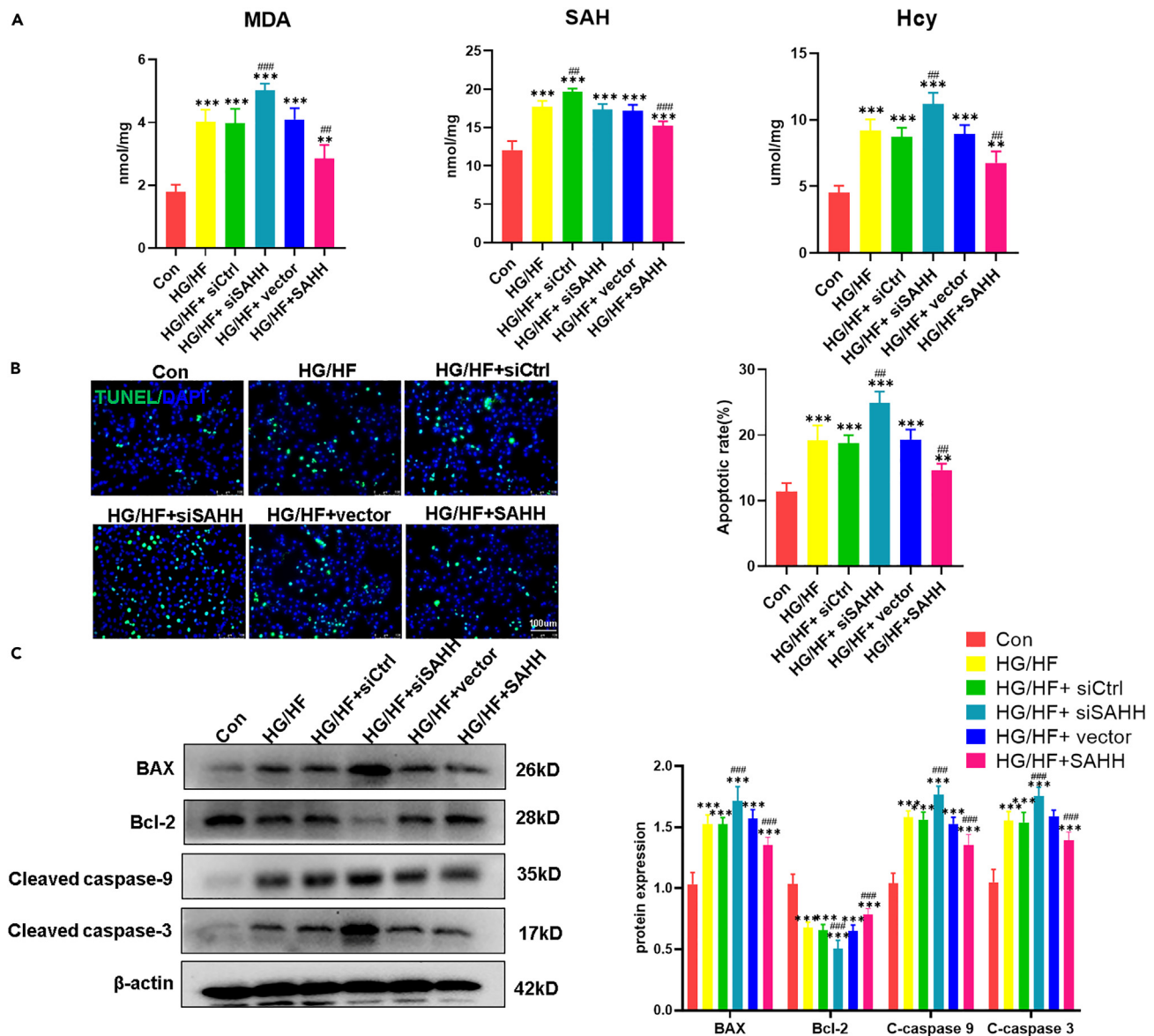
Figure 3. SAHH overexpression improved the SAH metabolism and antiapoptotic effect on HG/HF-induced cardiomyocytes *in vitro*

(A) Levels of the metabolites MDA (nmol/mg), SAH (nmol/mg), and Hcy (μmol/mg) were measured in the medium of H9C2 cells after treatment with HG/HF and *SAHH* overexpression (n = 5).

(B) TUNEL staining to assess the apoptotic index in H9C2 cells after treatment with HG/HF and *SAHH* overexpression (n = 5, scale bar: 100 μm).

(C) Apoptosis-related proteins were detected in H9C2 cells after treatment with HG/HF and *SAHH* overexpression (n = 4). *$p < 0.05$ versus Con group, #$p < 0.05$ versus HG/HF group.

Data in bar plots are presented as mean ± SD. **$p < 0.01$; ***$p < 0.001$ versus Con group, ##$p < 0.01$; ###$p < 0.001$ versus HG/HF group.

decreased in the hearts of rats in the DCM groups; these changes were considerably attenuated by DM+ov-SAHH delivery (Figure 7C). Thus, UTMD-mediated SAHH transfection delays the onset of cardiomyocyte apoptosis.

Antioxidative injury effects of SAHH on DCM

We examined whether SAHH was involved in this antioxidative effect. Mitochondria are the main source of ROS production. We observed that myocardial tissues from DCM rats showed a significant loss of mitochondrial membrane potential, which was improved by UTMD-mediated SAHH delivery (Figure 8A). We analyzed the level of heart oxidative stress using DHE fluorescent and 4-HNE staining and found that the cardiac delivery of SAHH further advanced the antioxidative effect in DCM hearts (Figures 8B and 8C). UTMD-mediated cardiac delivery of SAHH was demonstrated to prevent cardiac damage by decreasing the oxidative stress associated with myocardial injury.
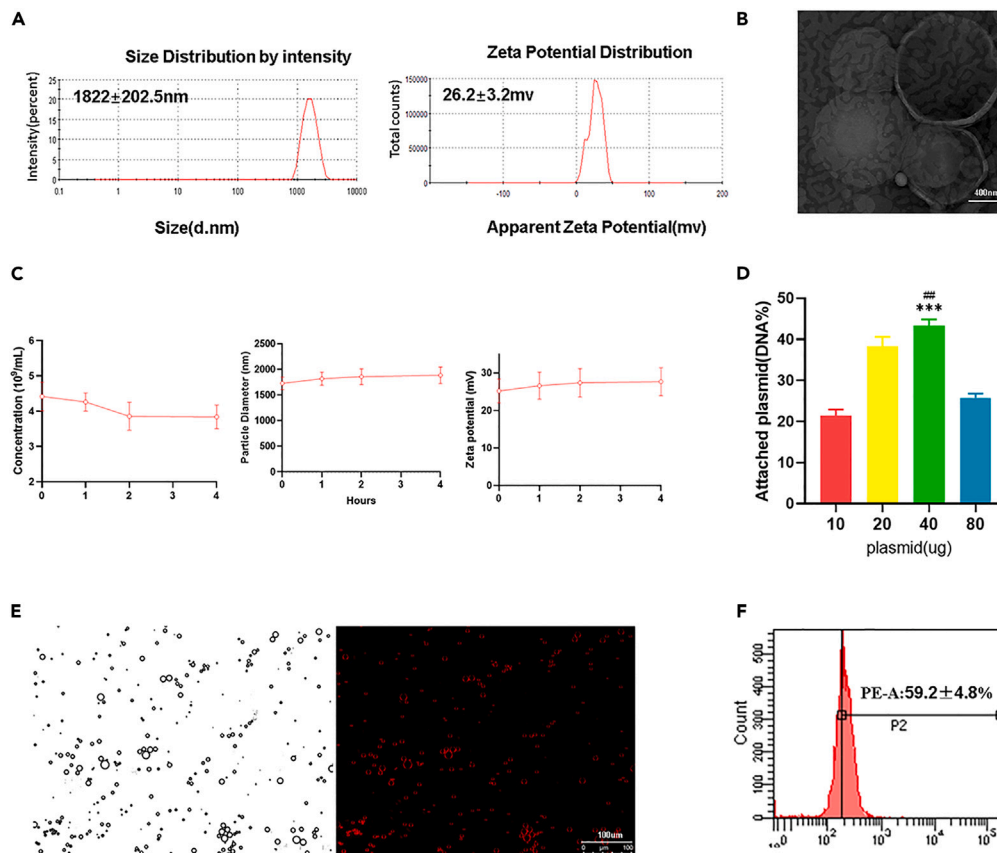
Figure 4. Preparation and assessment of plasmid/CMBs

(A) Size and zeta distribution of CMBs.

(B) Representative images of CMBs under a transmission electron microscope (scale bar: 400 nm).

(C) Concentration, size, and zeta potential of CMBs over 4 h at 25°C (n = 3).

(D) Binding percentage of different doses of DNA with CMBs (n = 3). *p < 0.05 versus 10 μg, #p < 0.05 versus 20 μg.

(E) Representative images of plasmid/CMBs. PI-labeled plasmids (red) merge with the outline of CMB (bright) (scale bar: 100 μm).

(F) Quantitative analysis of binding efficiency of plasmids with CMBs by flow cytometry.

Data in bar plots are presented as mean ± SD. ***p < 0.001 versus 10μg, ##p < 0.01 versus 20μg.

UTMD-mediated SAHH delivery improved myocardial injury and fibrosis in rats with DCM

One month after gene therapy, we euthanized the rats and histologically examined their heart tissues. We observed that the number of broken and swollen myocardial fibers in the hearts of the SAHH-overexpressing group was significantly less than that in the DCM group based on the injury score (Figure 9A). In addition, we found that the collagen deposition in the hearts of the SAHH-overexpressing group was moderately decreased compared with that in the diabetic group (Figure 9B). Pathological Masson staining of the heart tissue showed that DCM was accompanied by obvious myocardial interstitial fibrosis; whereas a significant reduction in the degree of fibrosis was found in the heart of rats after UTMD-mediated SAHH delivery (Figure 9C). These data demonstrated that localized myocardial UTMD-mediated delivery of SAHH plasmids protected the heart from DCM and thus improved cardiac remodeling.

UTMD-mediated delivery of SAHH alleviated cardiomyocyte hypertrophy and improved cardiac function

Semiquantitative analysis of the myocyte area using wheat germ agglutinin (WGA) staining revealed the presence of hypertrophic cardiomyocytes in the hearts of DCM rats; however, cardiomyocyte hypertrophy was moderately decreased in the SAHH-overexpressing group (Figure 10A). We performed an echocardiographic examination to investigate the cardiac function (Figure 10B). Echocardiography indicators suggested that overexpression of *SAHH* improved the cardiac function in rats, including left ventricular ejection fraction (LVEF), fractional shortening (FS), and E'/A', compared with that in DCM rats (Figures 10B–10D). However, UTMD-mediated CMB delivery of SAHH resulted in the greatest increase in ventricular function.
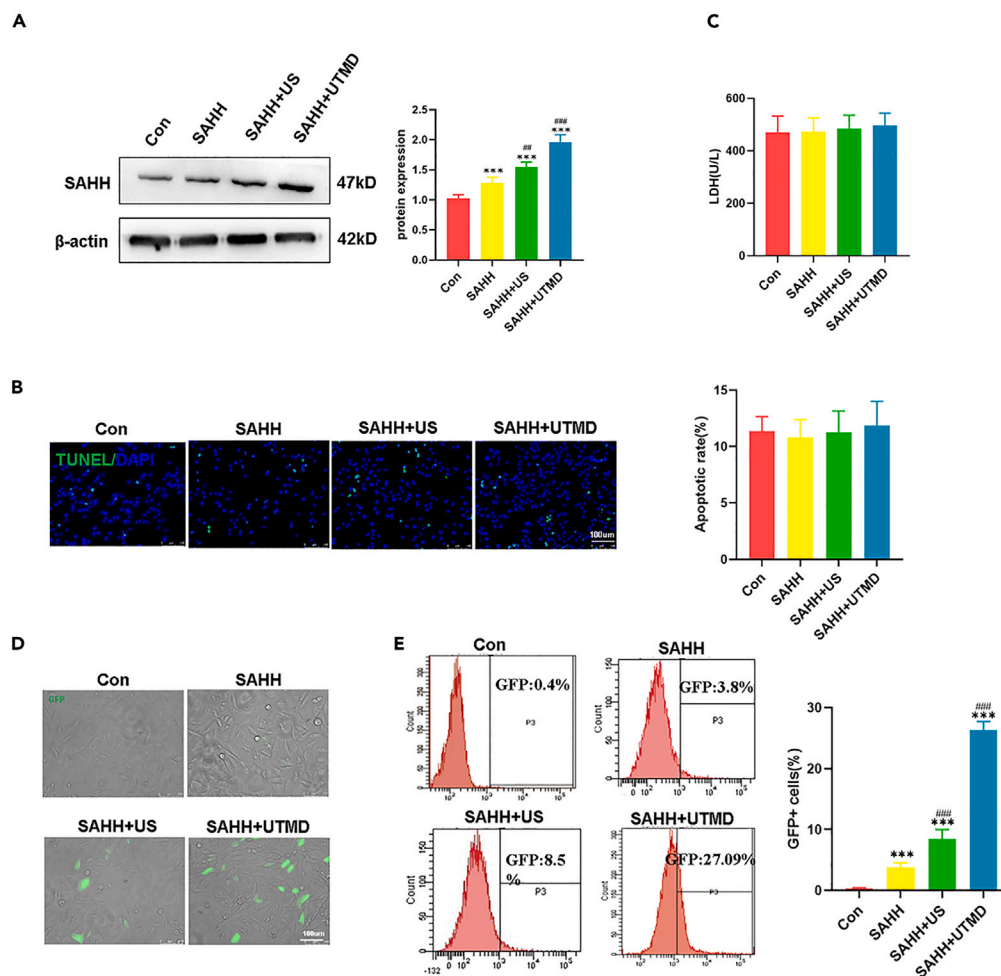
Figure 5. Transfection efficiency and safety of the uptake of SAHH plasmid/CMBs by H9C2 cells *in vitro*

(A) Western blotting and quantification of UTMD-mediated *SAHH* gene transfection in H9C2 cells for 48 h (n = 4).

(B) TUNEL staining to assess the apoptotic index in H9C2 cells after UTMD-mediated *SAHH* gene transfection (n = 4, scale bar: 100 μm).

(C) Levels of LDH (a marker of cellular injury) in the supernatants of H9C2 cells were evaluated using commercial kits before and after UTMD treatment (n = 5).

(D) Fluorescence images of successful GFP plasmid transfection dependent on UTMD technique; green for GFP (scale bar: 100 μm).

(E) Transfection efficiency of H9C2 cells as detected using flow cytometry after UTMD treatment (n = 4).

Data in bar plots are presented as mean ± SD. ***$p < 0.001$ versus Con group, $^{##}p < 0.01$; $^{###}p < 0.001$ versus SAHH group.

SAHH overexpression activated AMPK-mediated antioxidative injury and improved the biological activity of H9C2 cells induced by HG/HF

AMPK activation is usually associated with cell survival pathways, with AMPK playing a role in protecting cells from oxidative injury. We further explored whether SAHH activates the AMPK-mediated antioxidant pathway to improve the activity and function of HG/HF-induced H9C2 cells. We determined that *SAHH* overexpression upregulated the expression of p-AMPK, whereas treatment with an inhibitor of AMPK (compound C) had the opposite effect (Figure 11A). Therefore, we assumed that SAHH may improve the biological activity of H9C2 cells by promoting the expression of AMPK. As expected, *SAHH* overexpression upregulated the expression of the FOXO3 and SIRT3 proteins (Figure 11B). However, pretreatment with compound C abrogated the antioxidant effects of *SAHH* overexpression (Figure 11B). We next used the TUNEL assay to assess the level of apoptosis of H9C2 cells. We observed that *SAHH* overexpression had a significant antiapoptotic effect, whereas compound C attenuated this SAHH-mediated antiapoptotic effect (Figure 11C). We also used DHE staining (red) to evaluate the level of ROS in SAHH-overexpressing H9C2 cells. We found that *SAHH* overexpression increased the expression of AMPK and produced antioxidant effects, which were weakened by compound C (Figure 11D). These findings showed that SAHH is very important for improving the viability and biological functions of HG/HF-induced H9C2 cells, partly by regulating the AMPK-mediated antioxidant signaling pathway.
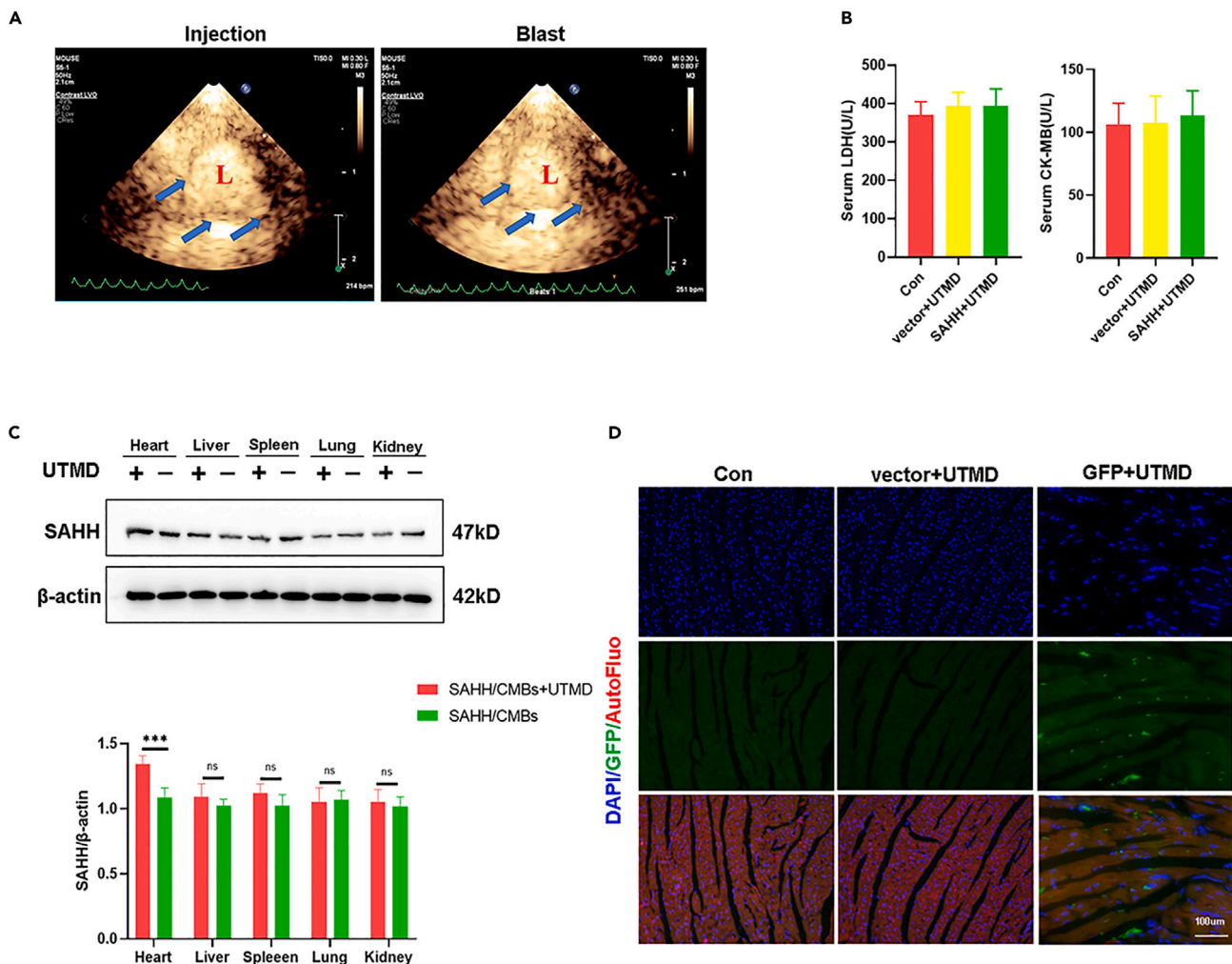
Figure 6. Transfection efficiency and safety of the cardiac uptake of SAHH plasmid/CMBs *in vivo*

(A) Representative ultrasound contrast images of CMBs in the heart after plasmid/CMB injection and ultrasound-targeted microbubble blast (L: left ventricle; arrows indicate the left ventricular wall).

(B) Serum levels of LDH (a marker of cellular injury) and CK-MB (a marker of myocardial injury) were evaluated using commercial kits before and after CMB injection and UTMD treatment (n = 5). The CMBs+UTMD×3 group was given three repeated UTMD treatments at one-day intervals: first, third, and fifth day. Blood sample was collected 6 h after the operation.

(C) Western blotting and quantification of the expression of SAHH in multiple organs (n = 4). *p < 0.05 versus SAHH+CMBs+UTMD group.

(D) Fluorescence images of successful GFP plasmid transfection dependent on the UTMD technique, DAPI for nucleus; green for GFP (scale bar: 100 μm).

Data in bar plots are presented as mean ± SD. ***p < 0.001 versus SAHH/CMBs+UTMD, ns: p ≥ 0.05.

DISCUSSION

In this study, we describe a novel gene delivery technique, UTMD, combined with CMBs used to increase the efficiency of *SAHH* gene delivery in rat myocardial cells (H9C2) and a DCM rat model. Using UTMD, we demonstrated that CMBs successfully delivered the *SAHH* gene in DCM rats, significantly decreasing oxidative stress injury and apoptosis, alleviating cardiomyocyte hypertrophy, increasing antifibrotic activity, and enhancing cardiac function. The levels of the myocardial phospho-AMPK protein and its downstream targets FOXO3 and SIRT3 were significantly increased following the UTMD-mediated delivery of SAHH, indicating successful gene expression and signaling.

The delivery of gene therapy in DCM has shown promising preliminary results in improving left ventricle systolic function and attenuating oxidative stress and cardiac remodeling.[16,17] However, low targeting and specificity greatly limit the efficacy of gene therapy. The current methods for gene delivery include viral and nonviral vectors.[18] Viral vectors are limited by their complexity, cost, and immunogenicity,[19] whereas nonviral vector-naked plasmid DNA (pDNA) transfer is simple and less immunogenic; however, the intravenous injection of naked DNA is associated with low transfection efficiency.[20] UTMD technology has been demonstrated to be a promising method for noninvasive, nonviral, and repeatable alternative targeted delivery.[11]
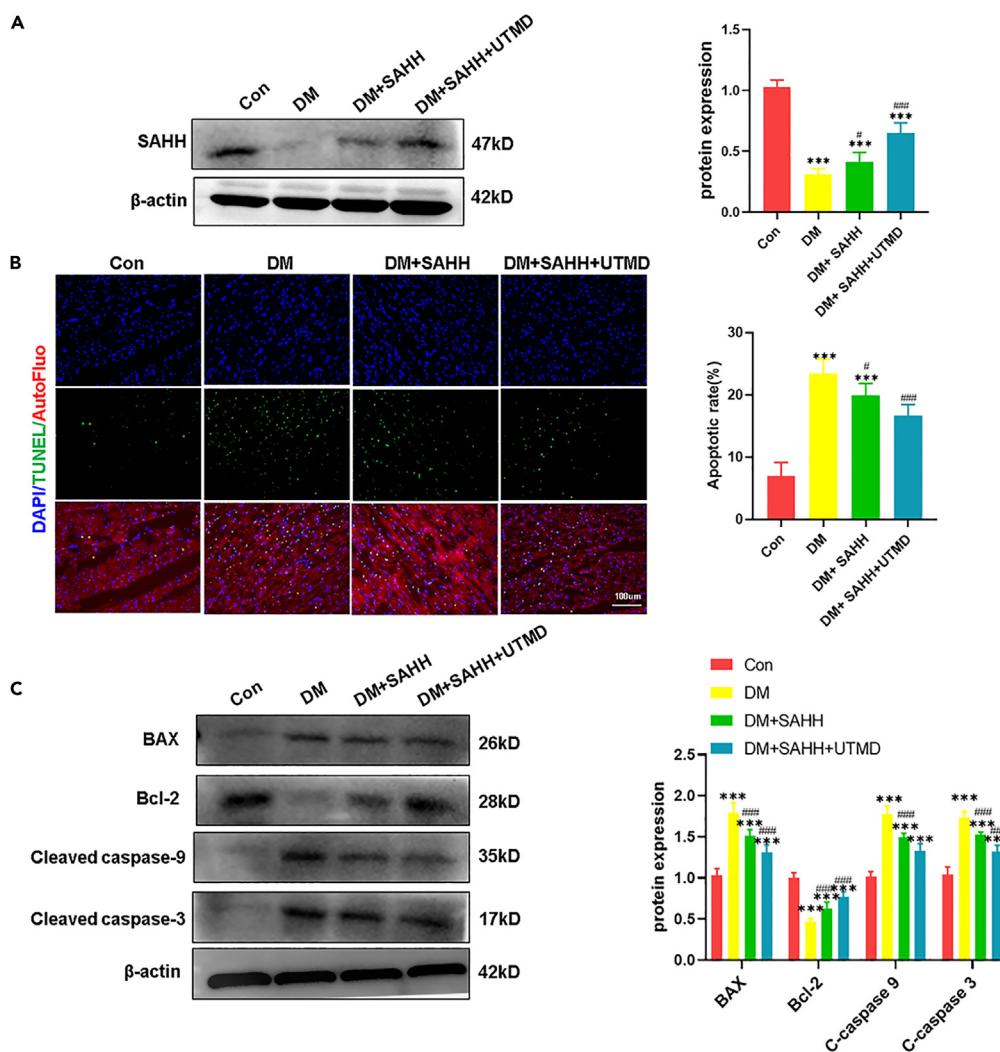
Figure 7. SAHH/CMB treatment increased transfection efficiency and decreased the rates of myocardial cell apoptosis in rats with diabetic cardiomyopathy

(A) Western blotting and quantification of UTMD-mediated *SAHH* gene transfection in rats with diabetic cardiomyopathy (n = 5). The CMBs+UTMD×3 group was given three repeated UTMD treatments at one-day intervals: first, third, and fifth day. Myocardial tissue was collected 1 month after treatment.

(B) Representative TUNEL staining images of heart sections; cardiomyocytes were labeled with autofluorescence, while cell nuclei were stained with DAPI (n = 5; scale bar: 100 μm).

(C) Apoptosis-related proteins were detected in myocardial tissue after UTMD-mediated SAHH gene transfection in rats (n = 4).

Data in bar plots are presented as mean ± SD. ***p < 0.001 versus Con group, #p < 0.05; # # #p < 0.001 versus DM group.

Recently, UTMD technology has been reported as a valuable treatment approach for targeted drug delivery in clinical trials.[13,14] In our study, UTMD significantly enhanced the transfection of the *SAHH* gene in cardiac tissues using CMB target blasting. We used relatively low ultrasound frequencies between 1 and 3 MHz, as low ultrasound frequencies facilitate a controllable and local transfection, thus promoting gene transfection into cells and tissues.[21] These findings support the prospect that UTMD can achieve specific gene delivery to cardiac targets, with good feasibility and promising clinical translation prospects for clinical applications.[6,22] Indeed, translational research using large animals revealed that UTMD has great prospects for application in gene therapy as indicated by the results in porcine myocardial hypertrophy models.[12] Several genes have been shown to improve cardiac function and cardiomyopathy in diabetic rats, with *SAHH* recently receiving increased attention.

SAHH is a cellular enzyme responsible for catalyzing the hydrolysis of SAH to adenosine and homocysteine.[23] Inhibition of SAHH via genetic or pharmacological intervention in mice elevated the plasma levels of SAH and induced endothelial dysfunction, thereby promoting atherosclerosis development.[24] Inhibition of SAHH was also shown to lead to SAH accumulation and promote high glucose-induced podocyte injury, thus inducing TXNIP-mediated oxidative stress and the activation of the NLRP3 inflammasome, ultimately accelerating diabetic
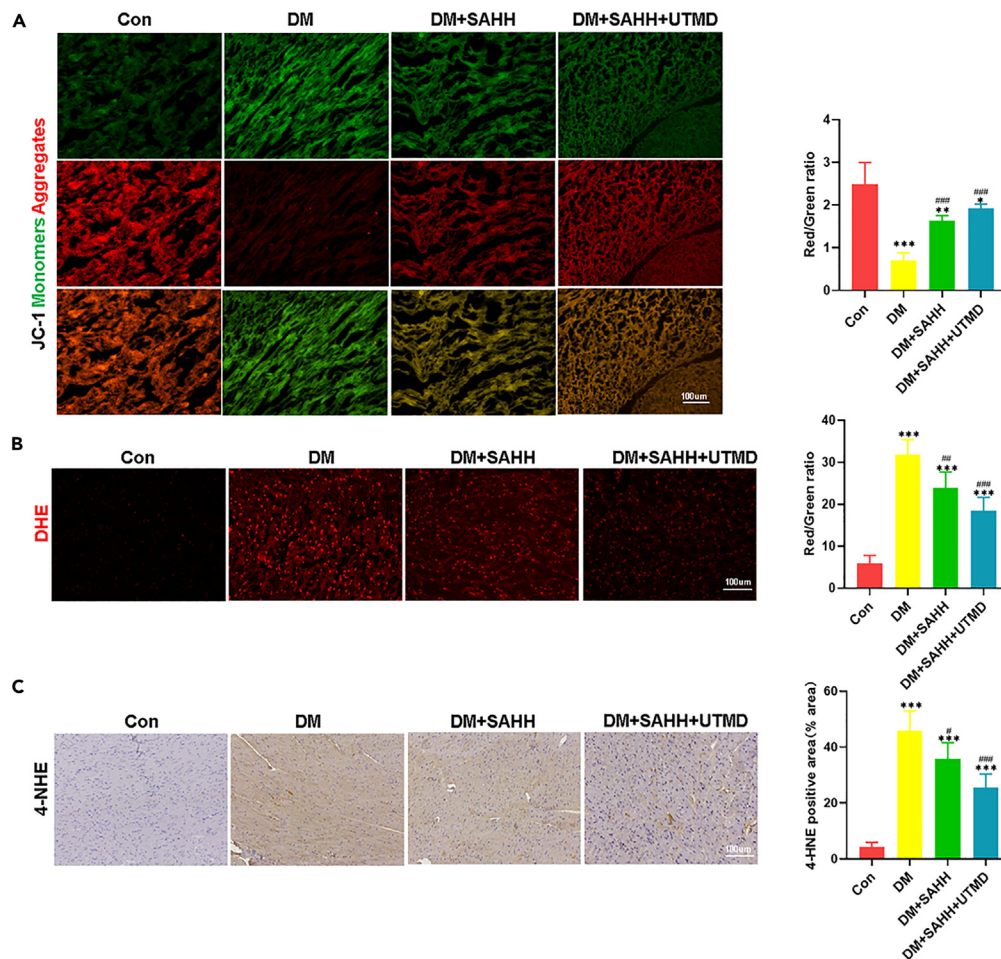
Figure 8. UTMD-mediated *SAHH* overexpression treatment enhanced the antioxidant effect in rats with diabetic cardiomyopathy
(A) JC-1 staining of heart sections treated with or without UTMD-mediated *SAHH* gene transfection. The ratio of JC-1 aggregates (red) in healthy mitochondria and JC-1 monomers (green) in depolarized mitochondria was used to assess the mitochondrial membrane potential (n = 5; scale bar: 100 μm).
(B) DHE staining in heart sections treated with or without UTMD-mediated *SAHH* gene transfection. Quantification of DHE intensity reflecting the myocardial levels of ROS (n = 5; scale bar: 100 μm).
(C) 4-NHE immunohistochemical staining in heart sections treated with or without UTMD-mediated *SAHH* gene transfection. Quantification of the concentration of 4-NHE reflecting the myocardial level of oxidative stress (n = 5; scale bar: 100 μm).
Data in bar plots are presented as mean ± SD. *p < 0.05;**p < 0.01; ***p < 0.001 versus Con group, #p < 0.05; ##p < 0.01; ###p < 0.001 versus DM group.

nephropathy.[7] Ling et al.[8,25–27] reported that the DNA methylation of p66shc is regulated by SAHH, with SAHH inhibition inducing endothelial dysfunction; p66shc exerts its effect through both replicative aging and stress-induced premature aging of hepatocytes, endothelial cells, and renal tubular cells. In our experiments, the expression of SAHH was decreased in both *in vitro* and *in vivo* DCM models. This evidence suggests that the *SAHH* gene is critical for maintaining redox homeostasis in diabetes.[28]

SAHH overexpression significantly improved the biological activity and function of HG/HF-treated H9C2 cells. In DCM, SAHH is not expressed or activated properly, further inhibiting the AMPK-mediated antioxidant activity. Moreover, SAHH deficiency resulted in lower intracellular levels of adenosine and reduced activation of AMPK, thus abolishing the osteoblastic differentiation of VSMCs and their ability to repair atherosclerotic calcification.[6] Increasing the activity of SAHH reportedly improved diabetic abnormalities in bone marrow-derived mesenchymal stem cells and increased their therapeutic effect in DCM.[28] In the current study, UTMD-mediated delivery of SAHH increased myocardial levels of phospho-AMPK and its downstream target proteins FOXO3 and SIRT3, whereas the AMPK inhibitor, compound C, increased apoptosis and attenuated antioxidant injury. Importantly, our data demonstrated that UTMD-mediated delivery of the SAHH-containing plasmid resulted in a significantly greater efficiency of gene transfection. Therefore, this UTMD-mediated gene transfer method can be clinically used to improve gene delivery to target organs.

In summary, our study found that the levels of SAHH were significantly decreased in DCM. UTMD-mediated cardiac delivery of the *SAHH* gene optimized its antioxidative effects in DCM. We demonstrated that CMBs enhanced gene transfection and improved cardiac function. UTMD-mediated *SAHH* transfection may be an important advancement in cardiac gene therapy for restoring ventricular function after DCM.
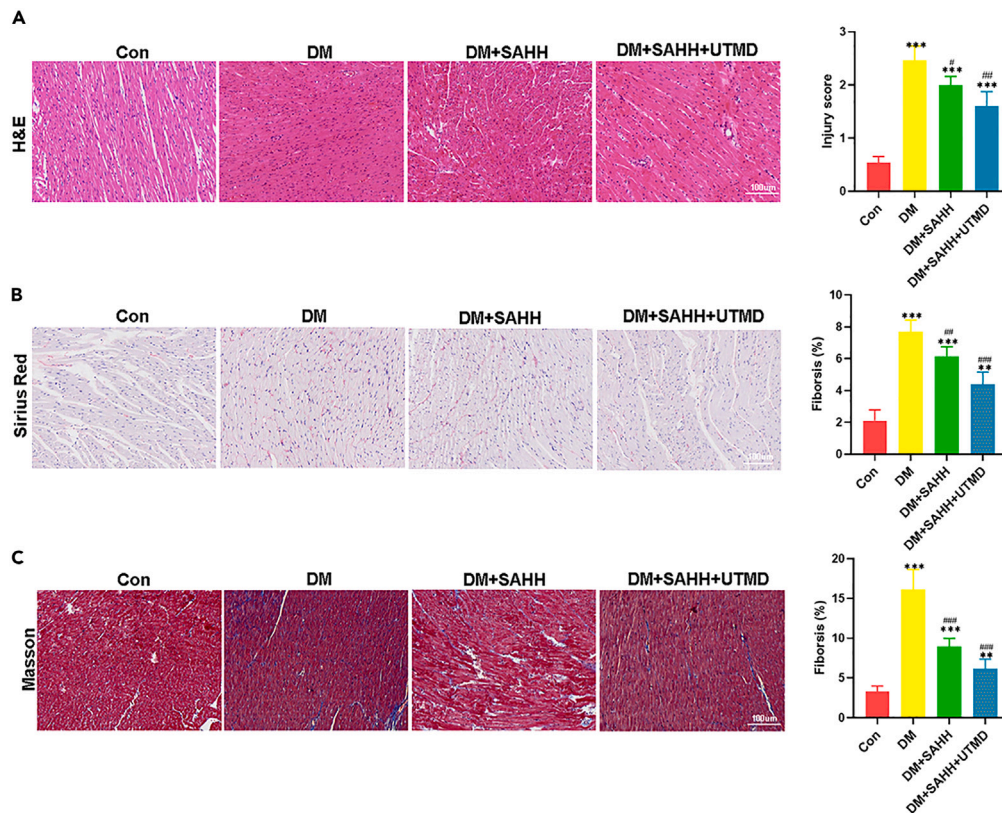
Figure 9. UTMD-mediated *SAHH* overexpression treatment alleviated myocardial damage and fibrosis in rats with diabetic cardiomyopathy
(A) Representative hematoxylin and eosin (H&E) staining of heart sections (n = 5; scale bar: 100 μm).
(B) Representative Sirius Red staining of heart sections (n = 5; scale bar: 100 μm).
(C) Representative Masson staining of heart sections (n = 5; scale bar: 100 μm). $*p < 0.05$ versus Con group, $\#p < 0.05$ versus DM group.
Data in bar plots are presented as mean ± SD. $**p < 0.01$; $***p < 0.001$ versus Con group, $\#p < 0.05$; $\#\#p < 0.01$; $\#\#\#p < 0.001$ versus DM group.

Limitations of the study

Our study had certain limitations. The binding of plasmids and microbubbles can be detected using simulated hemodynamic functions and animal characteristics. However, owing to the limitations of the experimental conditions, we only calculated the average binding ratio of plasmids and microbubbles in the collected supernatant milky-white layer and lower clear layer after centrifugation. Another limitation is that a mixture of microbubbles and plasmids is naturally trapped by the reticuloendothelial system and is mainly phagocytosed by macrophages in the spleen and liver. Owing to their proximity to the heart, partial irradiation of the spleen and liver eventually leads to the elevated expression of target genes in the spleen and liver.[15] We hope to design more accurate probes in the future so that ultrasound can focus more on specific organs. Finally, we observed that the SAHH-mediated activation of the AMPK/FOXO3/SIRT3 signaling pathway led to the recovery of the redox balance and improved cardiac function. However, the details of this mechanism require further investigation.

We showed that CMBs improved UTMD-mediated gene transfection; however, particular modifications are still required, including the development of nanocomplex-conjugated microbubbles, which will further enhance the stability or delivery efficiency and increase transgene expression in the target area.[29] UTMD-mediated gene therapy is a promising approach in the field of medicine, with potential utility not only in cardiology and cardiovascular therapies[12,15] but also in the treatment of tumors.[30]

STAR★METHODS

Detailed methods are provided in the online version of this paper and include the following:

- KEY RESOURCES TABLE
- RESOURCE AVAILABILITY
  - Lead contact
  - Materials availability
  - Data and code availability
- EXPERIMENTAL MODEL AND SUBJECT DETAILS
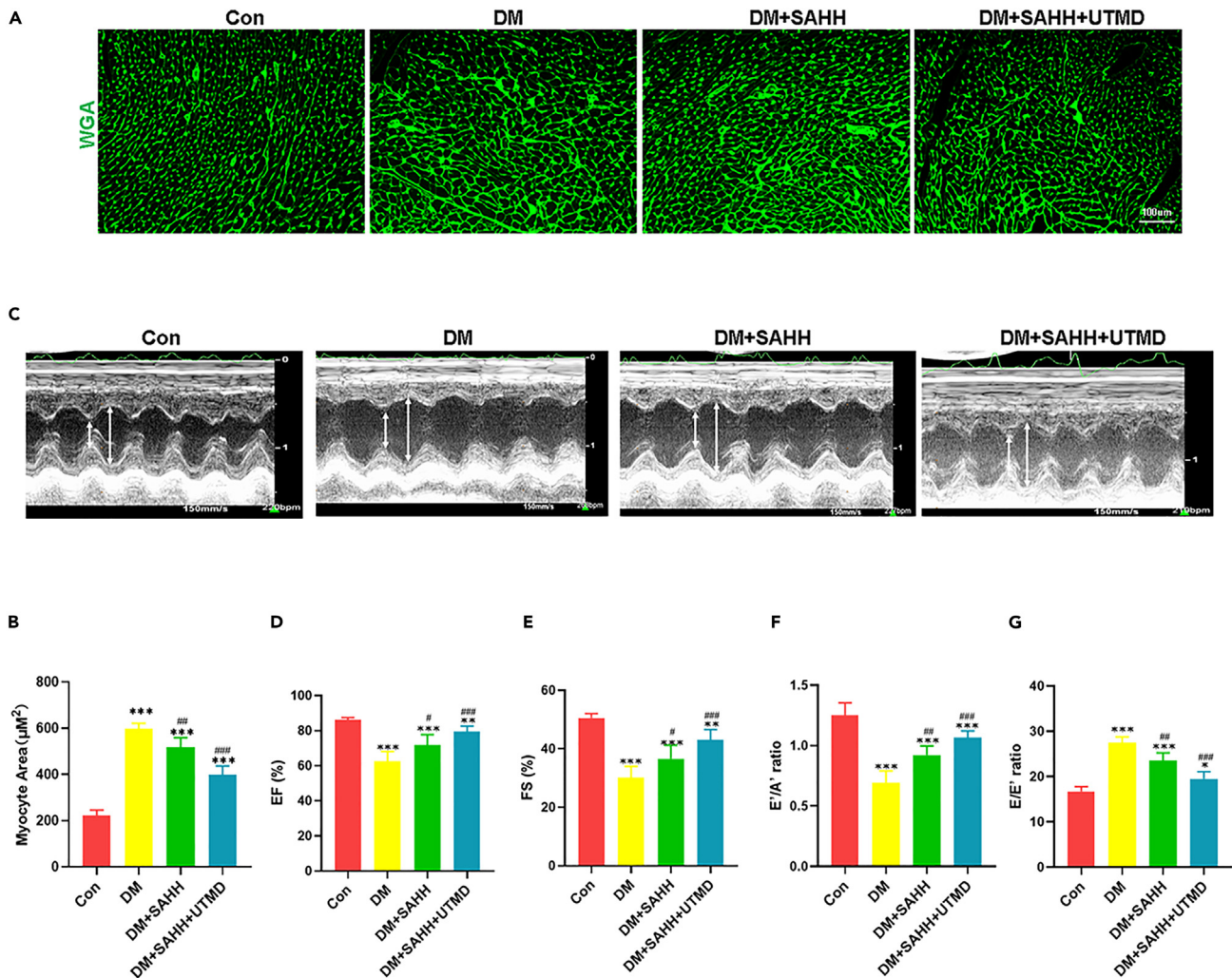
Figure 10. UTMD-mediated *SAHH* overexpression treatment alleviated cardiomyocyte hypertrophy and improved cardiac function in rats with diabetic cardiomyopathy

(A) Wheat germ agglutinin (WGA) staining was performed to estimate cardiomyocyte (CM) hypertrophy (n = 5; scale bar: 100 μm).

(B) Representative echocardiography images of heart sections treated with or without UTMD-mediated *SAHH* gene transfection (high lines: LVEDd; low lines: LVESd).

(C–G) Left ventricular ejection fraction (LVEF), left ventricular fraction shortening (LVFS), E'/A' ratio and E'/E' ratio were calculated (n = 5).

Data in bar plots are presented as mean ± SD. *$p < 0.05$; **$p < 0.01$; ***$p < 0.001$ versus Con group, #$p < 0.05$; ##$p < 0.01$; ###$p < 0.001$ versus DM group.

- ○ Cell culture
- ○ Animals
- ● METHOD DETAILS
  - ○ Preparation of CMBs
  - ○ Construction of plasmid-CMBs
  - ○ Cell transfection
  - ○ Ultrasound-mediated gene transfection with CMBs *in vitro*
  - ○ Gene delivery using UTMD *in vivo*
  - ○ RT-qPCR
  - ○ Western blotting
  - ○ Apoptosis assessment
  - ○ Reactive oxygen species assessment
  - ○ Mitochondrial membrane potential
  - ○ Pathological analysis
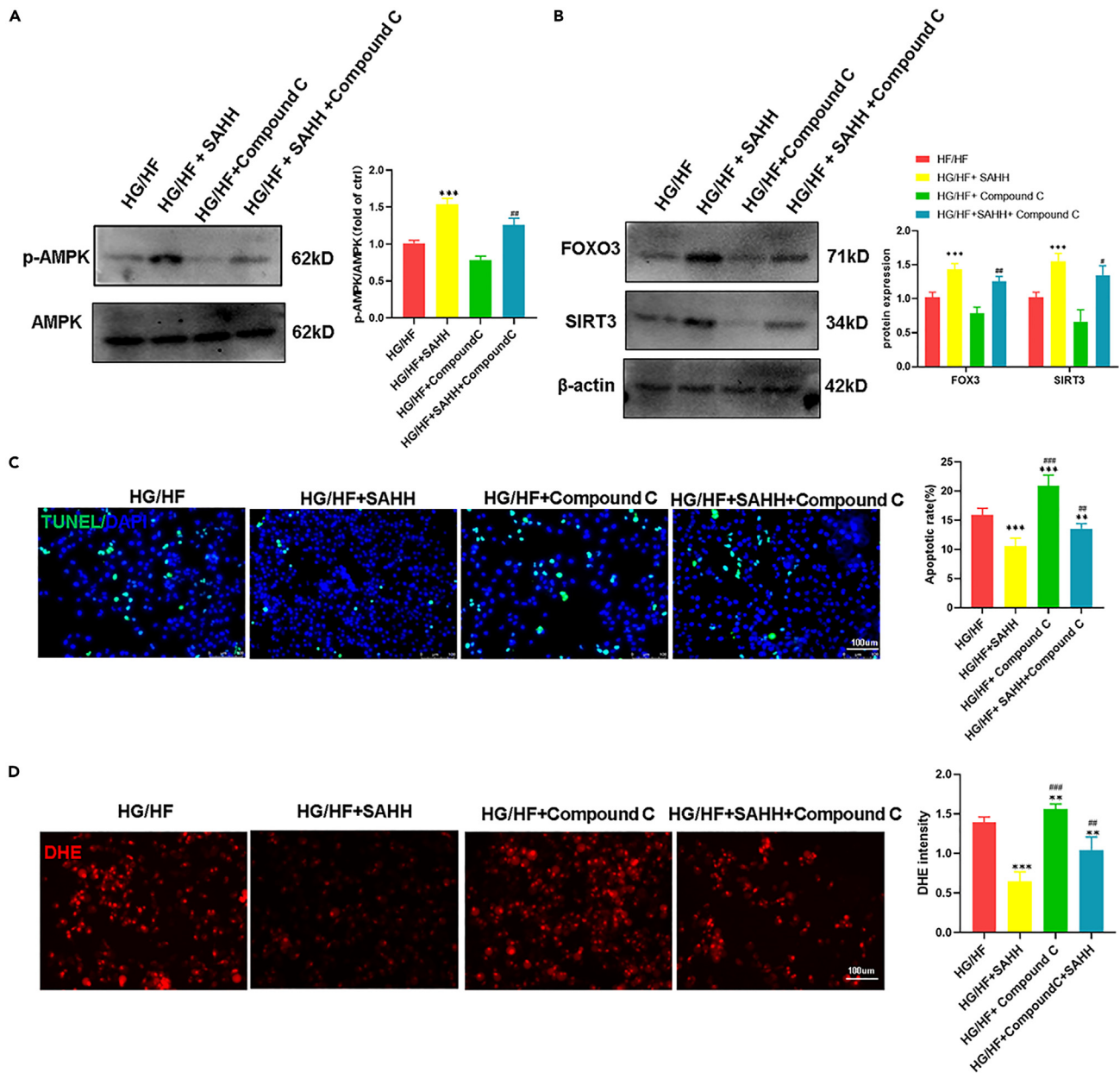
Figure 11. UTMD-mediated *SAHH* overexpression treatment is partly achieved through the activation of the AMPK-mediated antioxidant signaling pathway

(A) AMPK protein expression was assessed in HG/HF-induced H9C2 cells after *SAHH* overexpression and administration of compound C (AMPK inhibitor) (n = 5).

(B) Levels of downstream molecules, including antioxidative FOXO3 and SIRT3, were measured using western blotting (n = 5).

(C) TUNEL staining to assess the apoptosis index in HG/HF-induced H9C2 cells after *SAHH* overexpression and administration of compound C (n = 5, scale bar: 100 μm).

(D) DHE immunofluorescence staining in HG/HF-induced H9C2 cells after *SAHH* overexpression and administration of compound C (n = 5, scale bar: 100 μm). *$p < 0.05$ versus HG/HF group, #$p < 0.05$ versus HG/HF + SAHH group.

Data in bar plots are presented as mean ± SD. **$p < 0.01$; ***$p < 0.001$ versus HG/HF group, #$p < 0.05$; ##$p < 0.01$; ###$p < 0.001$ versus HG/HF + SAHH group.

○ Enzyme-linked immunosorbent assay kits
○ Echocardiography
● QUANTIFICATION AND STATISTICAL ANALYSIS

REFERENCES

1. Wu, Y., Ding, Y., Tanaka, Y., and Zhang, W. (2014). Risk factors contributing to type 2 diabetes and recent advances in the treatment and prevention. Int. J. Med. Sci. *11*, 1185–1200.

2. Tan, Y., Zhang, Z., Zheng, C., Wintergerst, K.A., Keller, B.B., and Cai, L. (2020). Mechanisms of diabetic cardiomyopathy and potential therapeutic strategies: preclinical and clinical evidence. Nat. Rev. Cardiol. *17*, 585–607.

3. Palmer, J.L., and Abeles, R.H. (1979). The mechanism of action of s-adenosylhomocysteinase. J. Biol. Chem. *254*, 1217–1226.

4. Kerins, D.M., Koury, M.J., Capdevila, A., Rana, S., and Wagner, C. (2001). Plasma s-adenosylhomocysteine is a more sensitive indicator of cardiovascular disease than plasma homocysteine. Am. J. Clin. Nutr. *74*, 723–729.

5. Castro, R., Rivera, I., Struys, E.A., Jansen, E.E.W., Ravasco, P., Camilo, M.E., Blom, H.J., Jakobs, C., and Tavares de Almeida, I. (2003). Increased homocysteine and s-adenosylhomocysteine concentrations and dna hypomethylation in vascular disease. Clin. Chem. *49*, 1292–1296.

6. Dai, X., Liu, S., Cheng, L., Huang, T., Guo, H., Wang, D., Xia, M., Ling, W., and Xiao, Y. (2022). Epigenetic upregulation of h19 and ampk inhibition concurrently contribute to s-adenosylhomocysteine hydrolase deficiency-promoted atherosclerotic calcification. Circ. Res. *130*, 1565–1582.

7. Dai, X., Liao, R., Liu, C., Liu, S., Huang, H., Liu, J., Jin, T., Guo, H., Zheng, Z., Xia, M., et al. (2021). Epigenetic regulation of txnip-mediated oxidative stress and nlrp3 inflammasome activation contributes to sahh inhibition-aggravated diabetic nephropathy. Redox Biol. *45*, 102033.

8. You, Y., Sun, X., Xiao, J., Chen, Y., Chen, X., Pang, J., Mi, J., Tang, Y., Liu, Q., and Ling, W. (2022). Inhibition of s-adenosylhomocysteine hydrolase induces endothelial senescence via htert downregulation. Atherosclerosis *353*, 1–10.

9. Hermes, M., Osswald, H., Riehle, R., Piesch, C., and Kloor, D. (2008). S-adenosylhomocysteine hydrolase overexpression in hek-293 cells: effect on intracellular adenosine levels, cell viability, and dna methylation. Cell. Physiol. Biochem. *22*, 223–236.

10. Ishikawa, K., Weber, T., and Hajjar, R.J. (2018). Human cardiac gene therapy. Circ. Res. *123*, 601–613.

11. Sun, L., Huang, C.W., Wu, J., Chen, K.J., Li, S.H., Weisel, R.D., Rakowski, H., Sung, H.W., and Li, R.K. (2013). The use of cationic microbubbles to improve ultrasound-targeted gene delivery to the ischemic myocardium. Biomaterials *34*, 2107–2116.

12. Qin, X., Cai, P., Liu, C., Chen, K., Jiang, X., Chen, W., Li, J., Jiao, X., Guo, E., Yu, Y., et al. (2023). Cardioprotective effect of ultrasound-targeted destruction of sirt3-loaded cationic microbubbles in a large animal model of pathological cardiac hypertrophy. Acta Biomater. *164*, 604–625.

13. Carpentier, A., Canney, M., Vignot, A., Reina, V., Beccaria, K., Horodyckid, C., Karachi, C., Leclercq, D., Lafon, C., Chapelon, J.Y., et al. (2016). Clinical trial of blood-brain barrier disruption by pulsed ultrasound. Sci. Transl. Med. *8*, 343re2.

14. Omata, D., Unga, J., Suzuki, R., and Maruyama, K. (2020). Lipid-based microbubbles and ultrasound for therapeutic application. Adv. Drug Deliv. Rev. *154–155*, 236–244.

15. Wang, S., Chen, K., Wang, Y., Wang, Z., Li, Z., Guo, J., Chen, J., Liu, W., Guo, X., Yan, G., et al. (2023). Cardiac-targeted delivery of nuclear receptor roralpha via ultrasound targeted microbubble destruction optimizes the benefits of regular dose of melatonin on sepsis-induced cardiomyopathy. Biomater. Res. *27*, 41.

16. Prakoso, D., De Blasio, M.J., Tate, M., Kiriazis, H., Donner, D.G., Qian, H., Nash, D., Deo, M., Weeks, K.L., Parry, L.J., et al. (2020). Gene therapy targeting cardiac phosphoinositide 3-kinase (p110alpha) attenuates cardiac remodeling in type 2 diabetes. Am. J. Physiol. Heart Circ. Physiol. *318*, H840–H852.

17. Zhang, N., Yu, H., Liu, T., Zhou, Z., Feng, B., Wang, Y., Qian, Z., Hou, X., and Zou, J. (2023). Bmal1 downregulation leads to diabetic cardiomyopathy by promoting bcl2/ip3r-mediated mitochondrial ca2+ overload. Redox Biol. *64*, 102788.

18. Alzaraa, A., Gravante, G., Chung, W.Y., Al-Leswas, D., Bruno, M., Dennison, A.R., and Lloyd, D.M. (2012). Targeted microbubbles in the experimental and clinical setting. Am. J. Surg. *204*, 355–366.

19. Chou, L.Y.T., Ming, K., and Chan, W.C.W. (2011). Strategies for the intracellular delivery of nanoparticles. Chem. Soc. Rev. *40*, 233–245.

20. Oyama, N., Takahashi, H., Kawaguchi, M., Miyamoto, H., Nishida, K., Tsurumaru, M., Nakashima, M., Yamashita, F., Hashida, M., and Kawakami, S. (2020). Effects of tissue pressure on transgene expression characteristics via renal local administration routes from ureter or renal artery in the rat kidney. Pharmaceutics *12*, 114.

21. Ilovitsh, T., Feng, Y., Foiret, J., Kheirolomoom, A., Zhang, H., Ingham, E.S., Ilovitsh, A., Tumbale, S.K., Fite, B.Z., Wu, B., et al. (2020). Low-frequency ultrasound-mediated cytokine transfection enhances t cell recruitment at local and distant tumor sites. Proc. Natl. Acad. Sci. USA *117*, 12674–12685.

22. Zhou, Y., Gu, H., Xu, Y., Li, F., Kuang, S., Wang, Z., Zhou, X., Ma, H., Li, P., Zheng, Y., et al. (2015). Targeted antiangiogenesis gene therapy using targeted cationic

microbubbles conjugated with cd105 antibody compared with untargeted cationic and neutral microbubbles. Theranostics 5, 399–417.

23. Wang, Y., Kavran, J.M., Chen, Z., Karukurichi, K.R., Leahy, D.J., and Cole, P.A. (2014). Regulation of s-adenosylhomocysteine hydrolase by lysine acetylation. J. Biol. Chem. 289, 31361–31372.

24. Xiao, Y., Xia, J., Cheng, J., Huang, H., Zhou, Y., Yang, X., Su, X., Ke, Y., and Ling, W. (2019). Inhibition of s-adenosylhomocysteine hydrolase induces endothelial dysfunction via epigenetic regulation of p66shc-mediated oxidative stress pathway. Circulation 139, 2260–2277.

25. Fu, B., Yang, J., Chen, J., Lin, L., Chen, K., Zhang, W., Zhang, J., and He, Y. (2019).

Preventive effect of shenkang injection against high glucose-induced senescence of renal tubular cells. Front. Med. 13, 267–276.

26. Zhang, J., Li, Y., Wang, B., Luo, Y., Shi, J., and Zhao, B. (2020). The p66shc-mediated regulation of hepatocyte senescence influences hepatic steatosis in nonalcoholic fatty liver disease. Med. Sci. Mon. Int. Med. J. Exp. Clin. Res. 26, e921887.

27. Zhang, H., Pang, X., Yu, H., and Zhou, H. (2022). Genistein suppresses ox-ldl-elicited oxidative stress and senescence in huvecs through the sirt1-p66shc-foxo3a pathways. J. Biochem. Mol. Toxicol. 36, e22939.

28. Wang, Y., Zhang, Y., Chen, K., Liu, J., Wu, D., Cheng, Y., Wang, H., and Li, Y. (2022). Insufficient s-adenosylhomocysteine

hydrolase compromises the beneficial effect of diabetic bmscs on diabetic cardiomyopathy. Stem Cell Res. Ther. 13, 418.

29. Li, X., Khorsandi, S., Wang, Y., Santelli, J., Huntoon, K., Nguyen, N., Yang, M., Lee, D., Lu, Y., Gao, R., et al. (2022). Cancer immunotherapy based on image-guided sting activation by nucleotide nanocomplex-decorated ultrasound microbubbles. Nat. Nanotechnol. 17, 891–899.

30. Wu, T., Huang, C., Yao, Y., Du, Z., and Liu, Z. (2022). Suicide gene delivery system mediated by ultrasound-targeted microbubble destruction: a promising strategy for cancer therapy. Hum. Gene Ther. 33, 1246–1259.

STAR★METHODS

KEY RESOURCES TABLE

REAGENT or RESOURCE	SOURCE	IDENTIFIER
Antibodies		
Rabbit monoclonal anti-SAHH	Abcam	Cat# ab134966
Rabbit monoclonal anti-p-AMPK	Abcam	Cat# ab32508; RRID: AB_722769
Rabbit monoclonal anti-AMPK	Abcam	Cat# ab32047; RRID: AB_722764
Rabbit polyclonal anti-FOXO3	Abcam	Cat# ab23683; RRID: AB_732424
Rabbit polyclonal anti-SIRT3	Abcam	Cat# ab189860
Rabbit monoclonal anti-BAX	Abcam	Cat# ab182734
Rabbit polyclonal anti-Bcl-2	Abcam	Cat# ab194583; RRID: AB_2783814
Rabbit polyclonal anti-cleaved caspase 9	Affinity	Cat# AF5240; RRID: AB_2837726
Rabbit polyclonal anti-cleaved caspase 3	Affinity	Cat# AF7022; RRID: AB_2835326
Mouse monoclonal anti-4 hydroxynonenal	R&D	Cat# MAB3249; RRID: MAB3249
Goat Anti-Rabbit IgG H&L (HRP)	Abcam	Cat# ab6721; RRID: AB_955447
Rabbit monoclonal anti-Anti-beta Actin	Abcam	Cat# ab115777: RRID: AB_10899528
Bacterial and virus strains		
DH5a	Beyotime	Cat# D1031S
Chemicals, peptides, and recombinant proteins		
Streptozotocin (STZ)	Sigma	Cat# 18883-66-4
DPPC	Avanti	Cat# 850355P-1G-A-321
DSPE-PEG2000	Avanti	Cat# 880160P-200MG-A-047
DC-Chol	Avanti	Cat# 700001P-200MG-B-021
compound C	Selleck	Cat# S7840
glycerol	Sigma	Cat# 56-81-5
DMEM	Sigma	Cat# D0822
FBS (fetal bovine serum)	ScienCell	Cat# 0500
TRIZOL	Invitrogen	Cat# 15596026
PI staining	Beyotime	Cat# ST511
PicoGreen fluorescent dye	Yeasen	Cat# 12641ES01
RIPA lysis buffer	Beyotime	Cat# P0013E
Critical commercial assays		
Situ Cell Death Detection Kit	Roche	Cat# 11684817910
cDNA synthesis kit	Roche	Cat# 04897030001
BCA Protein Assay Kit	Beyotime	Cat# P0012
PVDF membranes	Millipore	Cat# IPVH00010
LipofectamineTM 3000 Transfection Reagent	Invitrogen	Cat# L3000001
PrimeScript RT-PCR Kit	Takara	Cat# RR014A
Dihydroethidium (DHE)	Beyotime	Cat# S0063
JC-1 staining assay kit	Beyotime	Cat# C2005
hematoxylin and eosin	Solarbio	Cat# G1120
Masson stain	Solarbio	Cat# G1340
Sirius Red stain	Solarbio	Cat# G1473
wheat germ agglutinin (WGA)	Invitrogen	Cat# W11261
MDA ELISA Kit	Kselisa	Cat# KS13297

Continued

REAGENT or RESOURCE	SOURCE	IDENTIFIER
SAH ELISA Kit	Kselisa	Cat# KS13692
HCY ELISA Kit	Cusabio	Cat# CSB-E08896r
CK-MB ELISA Kit	Elabscience	Cat# E-EL-R1327c
LDH assay Kit	Beyotime	Cat# C0016
Experimental models: Cell lines		
H9C2	ATCC	RRID: CVCL_0286
Experimental models: Organisms/strains		
Eight-week-old Male SPF Sprague–Dawley rats	Harbin Medical University	RRID:RGD_1566457
Oligonucleotides		
Primers	See Table S1 for primers used in this study	N/A
Recombinant DNA		
pCMV6-AC-GFP	Origene	Cat# HG-VPO0901
pcDNA3.1(+)-SAHH	General Biol	Cat# MF29554
siRNA-SAHH	General Biol	Cat# RX084259
Software and algorithms		
ImageJ software	ImageJ	RRID:SCR_003070
GraphPad Prism 7.0	GraphPad Prism	RRID:SCR_002798
FlowJo	Tree Star	RRID:SCR_008520

RESOURCE AVAILABILITY

Lead contact

Further information and requests for resources and reagents should be directed to and will be fulfilled by the lead contact, Leiguang Feng (leiguangfeng@163.com).

Materials availability

This study did not generate new unique reagents. All unique/stable reagents generated in this study are available from the lead contact with a completed Materials Transfer Agreement.

Data and code availability

- All data reported in this paper will be shared by the lead contact upon request.
- This paper does not report original code.
- Any additional information required to reanalyze the data reported in this paper is available from the lead contact upon request.

EXPERIMENTAL MODEL AND SUBJECT DETAILS

Cell culture

Rat myocardial cells (H9C2, ATCC, Cat# CRL-1446, RRID: CVCL_0286) were cultured in high-glucose DMEM (Sigma-Aldrich) containing 10 % (v/v) fetal bovine serum (ScienCell, Los Angeles, CA, USA), and 100 units/mL of penicillin-100 mg/mL of streptomycin (HyClone, SV30010, Utah, USA). Cell lines were routinely monitored in our laboratory by microscopic morphology, while cell line authentication was verified before starting this study by short tandem repeat (STR) profiling, according to ATCC cell authentication testing service. A test for mycoplasma contamination was negative. H9C2 cells were cultured under normal conditions (5 % CO_2, 21 % O_2, and 74 % N_2) in a humidified incubator at 37 °C. H9C2 cells were treated with a high concentration of glucose (25 mM, HG) and 200 μM palmitic acid (PA) for 24 h to mimic the diabetic microenvironment.

Animals

The induced type 2 diabetes mellitus rat model was established. Male Sprague–Dawley rats (8 weeks old, weighing approximately 200 g, RRID: RGD_1566457, pathogen and virus free) were purchased from the Animal Center of the Second Affiliated Hospital of Harbin Medical University (Harbin, Heilongjiang, China) and randomly divided into two groups: Control and DCM. Briefly, rats in the control group were fed a normal chow diet containing 4 % fat, whereas those in the DCM group were fed a high-fat diet (HFD; 60 % kcal from fat) for eight weeks. The

rats were maintained in the SPF facility and fed with sterilized food and autoclaved water *ad libitum* under a 12-h light/dark cycle at 25°C. After one week of environmental adaptation, HFD-fed rats were administered a single intraperitoneal injection of STZ (25 mg/kg; Sigma-Aldrich, Saint Louis, MO, USA) to induce type 2 diabetes. The same dose of medication was administered three times in total on consecutive days. Rats with levels of blood glucose ≥ 16.7 mmol/L each of three or more times during a week of continuous monitoring of tail capillary blood glucose levels were considered to be diabetic. Rats were subjected to echocardiography 12 weeks after STZ injection. The study protocol was reviewed and approved by the Animal Care and Use Committee of the First Affiliated Hospital of Harbin Medical University.

METHOD DETAILS

Preparation of CMBs

Briefly, CMBs were produced using a thin-film hydration method. Dipalmitoyl-phosphatidylcholine (DPPC), 1,2-distearoyl-sn-glycerol-3-phosphoethanolamine-N-maleimide (polyethylene glycol) (DSPE-PEG2000), and 3- [N- (N,N-dimethyl-aminoethane)-carbamoyl] cholesterol (DC-Chol; all from Avanti Polar Lipids, Inc., Alabaster, AL, USA) were weighed and dissolved in chloroform at a mass ratio of 5:2:0.5. The organic solvent was removed by rotary evaporation (Shanghai Yarong, Shanghai, China) at 50°C until a thin, homogeneous lipid film was formed. A 0.5 mL glycerol solution (glycerol: phosphate-buffered saline (PBS) = 1:9, v/v; Sigma-Aldrich) was added to a round bottom flask at 42°C for 30 min and then transferred to a 1.5 mL tube. The tube was capped using a rubber plug. The air inside the tube was then replaced with octafluoropropane (C_3F_8; Tianjin Nuclear industry physicochemical Research Institute, Tianjin, China). The solutions were then mixed in an oscillator for 1 min to obtain the gas-filled CMBs. The prepared CMBs were diluted and adjusted to 1×10^9 MB/mL in PBS, sterilized by 60Co-γ radiation, and stored at 4°C until further use. The size distribution and zeta potential of CMBs were determined using a Zetasiz-er Nano ZS particle analyzer (Malvern, Worcestershire, UK).

Construction of plasmid-CMBs

The shape and size of CMBs were observed under an electron microscope, and the corresponding changes in concentration, particle size, and zeta potential were recorded for 4 h. The DNA-loading capacity of CMBs was evaluated by measuring the plasmid DNA bound to CMBs. Plasmid DNA containing either GFP or the *SAHH* gene (10, 20, 40, or 80 μg) was added to 5×10^8 CMBs and incubated for 15 min to ensure DNA adsorption. The samples were then centrifuged at 25°C for 5 min at 400 × *g* to form two layers: an upper, milky-white layer containing the microbubbles bound to the plasmid, and a lower, clear layer containing the unbound plasmid. The clear layer was filtered through a 0.45 μm pore filter and centrifuged at 10 000 × *g* for 5 min. PicoGreen fluorescent dye (1:200 dilution in Tris-EDTA (TE) buffer; Yeasen, Shanghai, China) was added to each sample and incubated for 5 min at 25°C. The concentration of the plasmid DNA was evaluated based on the fluorescence intensity of the unconjugated plasmid detected using a microplate reader. The DNA loading capacity of CMBs was evaluated by measuring the percentage of plasmid DNA bound to CMBs according to the following equation: (DNA_{total} - DNA_{free})/DNA_{total} × 100%; the plasmid payload mass in CMBs was defined according to the following equation: (DNA_{total} - DNA_{free})/CMB number. Finally, the milky-white layer was diluted using PBS and photographed under a fluorescence microscope (Leica, Wetzlar, Germany). We used PI staining (Beyotime, Shanghai, China) to verify the binding of plasmids to microbubbles; we accordingly observed red fluorescence around the microbubbles using fluorescence microscopy. The binding of plasmids to microbubbles was detected using flow cytometry (BD, Franklin Lakes, NJ, USA).

Cell transfection

The siRNAs for SAHH and the control siRNA were synthesized by General Biol (Anhui，China). The siRNA sequences of SAHH were listed in Table S1. A SAHH-overexpressing plasmid was constructed by inserting rat SAHH cDNAs (NM_017201.2) into a pcDNA3.1(+)-Amp vector plasmid (General Biol, Anhui，China).The H9C2 cells were transfected with double-stranded siRNAs and SAHH-overexpressing plasmids by using the Lipofectamine3000 transfection reagent (Invitrogen, CA, USA) according to the manufacturer's protocol. After transfection for 72 h, the cells and supernatant were collected for subsequent experiments. The H9C2 cells were treated with an inhibitor of AMPK (compound C, 1 μmol/L; Selleck, Shanghai, China) for 24h with or without SAHH plasmid to inhibit AMPK/FOXO3/SIRT3 pathway expression.

Ultrasound-mediated gene transfection with CMBs *in vitro*

H9C2 cells were seeded in 24-well plates (Corning, NY, USA) at a density of 4.0×10^4 cells/well and transfected after reaching approximately 70 % confluence. The *SAHH*-containing plasmid (15 μg) was added to 2×10^8 microbubbles, and the plasmid/CMB mixture was incubated at 25°C for 10 min. The mixture was then diluted with DMEM to a final volume of 800 μL. The transfection mixture was added to each well and incubated for 10 min in a humidified incubator. The wells were sealed with a rubber stopper and inverted in an incubator to keep CMBs in contact with cells. Samples were subjected to treatment by ultrasound (UGT 1025; CQMU, Chongqing, China) at 1 MHz, 1 W/cm², and a 50 % duty cycle (DC) for 30 s. After gene transfection, H9C2 cells were cultured in high-glucose DMEM containing 10 % fetal bovine serum (FBS). Transfection efficiency was evaluated using western blotting, fluorescence microscopy, and flow cytometry 48 h after transfection. Apoptosis was measured 48 h after transfection using the Situ Cell Death Detection Kit (Roche, Pleasanton, CA, USA) according to the manufacturer's protocol.

Gene delivery using UTMD *in vivo*

Plasmid DNA (0.20 mg/kg body weight) was incubated with CMBs at 25°C for 10 min according to the optimal rate of binding, and the mixture was subsequently diluted in saline to a total volume of 1.0 mL/rat. Rats were anesthetized with isoflurane (5% for induction, 1.0–2.5% for maintenance), and prepared plasmid/CMBs mixtures were injected through the tail vein (2.0 mL/h). The ultrasound pulses were delivered for 30 min using an EPIQ 7 system (Philips, Amsterdam, Netherlands) equipped with an S5-1 transducer. A layer of ultrasound gel was applied to the transducer, which was adjusted 2–3 cm above the myocardial level. A pulse with a high mechanical index of approximately 1.2–1.35 was administered with an electrocardiograph (ECG)-mediated trigger for ultrasound bursts at each fourth end-systole for 30 min. The UTMD-mediated *SAHH* delivery was repeated thrice at one-day intervals. Transfection efficiency was evaluated using western blotting and fluorescent microscopy 2 d after transfection.

RT-qPCR

Tissue RNA was extracted from the myocardial tissue of control or DCM rats, whereas cellular RNA was extracted from control or H9C2 cells induced with HG/HF. Total RNA was isolated using the TRIZOL reagent (Invitrogen, Carlsbad, CA, USA) and then reverse transcribed to cDNA using a first-strand cDNA synthesis kit (Roche, Basel, Switzerland). Target genes were amplified by quantitative real-time PCR (qRT-PCR) using a Sequence Detection system (Bio-Rad, Herakles, CA, USA). The relative levels of expression of target genes were calculated using the $2-\Delta\Delta CQ$ method and normalized to those of the housekeeping gene, β-actin. The primers used are listed in Table S1.

Western blotting

Total protein was extracted from H9C2 cells, heart, liver, spleen, lungs, and kidney tissues using the RIPA lysis buffer (Beyotime, Beijing, China) containing protease and phosphatase inhibitors. Protein concentrations were measured using the BCA Protein Assay Kit (Beyotime). Protein was separated by SDS-PAGE (10 % gels) and transferred onto 0.22 μm polyvinylidene fluoride (PVDF) membranes. Each membrane was then incubated at 4°C overnight with primary antibodies against SAHH (1:5,000; ab134966; Abcam, Shanghai, China), p-AMPK (1:5,000; ab133448; Abcam, Shanghai, China), AMPK (1:5,000; ab32047; Abcam, Shanghai, China), FOXO3 (1 μg/ml; ab23683; Abcam, Shanghai, China), SIRT3 (1:1,000; ab189860; Abcam, Shanghai, China), BAX (1:1,000; ab182734; Abcam, Shanghai, China), Bcl-2 (1:2,000; ab194583; Abcam, Shanghai, China), cleaved caspase 9 (1:1,000; AF5240; Affinity, Jiangsu, China), and cleaved caspase 3 (1:1,000; AF7022; Affinity, Jiangsu, China). After incubation with HRP-labeled secondary antibodies (1:10,000; ab6721; Abcam, Shanghai, China) at 37°C for 1 h, protein bands were visualized using a chemiluminescence imaging system (Tanon, Shanghai, China).

Apoptosis assessment

The apoptosis of H9C2 cells or apoptotic ratio in the myocardium was determined using a TUNEL assay according to the manufacturer's instructions (Roche). For each sample, apoptotic cardiomyocytes were evaluated in five randomly chosen fields per section and quantitated using the Image-Pro Plus 6.0 System (IPP) image analysis system by two blinded observers. The percentage of TUNEL-positive nuclei was calculated and defined as the apoptotic index.

Reactive oxygen species assessment

Dihydroethidium (DHE) staining was performed on H9C2 cells and frozen heart tissue sections to detect intracellular reactive oxygen species (ROS). H9C2 cells and frozen sections were equilibrated and washed with PBS for 10 min, followed by incubation with 10 μmol/L DHE (Beyotime, Shanghai, China) at 37°C in the dark for 30 min. After washing thrice in PBS, H9C2 cells and frozen heart tissue sections were observed under a fluorescence microscope.

Mitochondrial membrane potential

Mitochondrial membrane potential was measured using a JC-1 staining assay kit (Beyotime, Shanghai, China), following the manufacturer's instructions. JC-1 aggregates (red) in healthy mitochondria with high levels of mitochondrial membrane potential producing red fluorescence. Conversely, when mitochondrial membrane potential is decreased, JC-1 is found in its monomeric form, producing green fluorescence. H9C2 cells and frozen sections were equilibrated and washed with PBS for 10 min, followed by incubation with 10 μg/mL JC-1 at 37°C in the dark for 30 min. After washing thrice in PBS, H9C2 cells and frozen heart tissue sections were observed under a fluorescence microscope (Leika, Germany). Five random images were captured per sample to examine the fluorescence intensities of the J-monomers and J-aggregates.

Pathological analysis

Heart tissues were fixed with 4% paraformaldehyde at 25°C for 72 h, paraffin-embedded, and cut into 5-μm-thick sections. Heart sections were stained with hematoxylin and eosin, Masson stain, and Sirius Red stain (all from Solarbio, Beijing, China). Paraffin-embedded sections were dewaxed, blocked, and incubated with rabbit anti-4 hydroxynonenal antibodies (4HNE, 1:500; R&D, Shanghai, China) overnight at 4°C under humidified conditions. Subsequently, sections were incubated with HRP-labeled secondary antibodies (1:2000) at 25°C for 1 h. Diaminobenzidine (DAB) was used for visualization, and images were captured under an inverted Olympus IX70 microscope (Olympus, Beijing, China). For

histological analysis, the cross-sectional areas of myocytes and tissue sections were stained with wheat germ agglutinin (WGA; plasma membrane staining, Alexa Fluor 488 conjugated) and analyzed using the ImageJ software (NIH, Maryland, USA).

Enzyme-linked immunosorbent assay kits

The levels of MDA, SAH, and Hcy in the H9C2 cell culture medium were determined using commercial enzyme-linked immunosorbent assay (ELISA) kits (Kselisa and Cusabio, China) according to the manufacturer's instructions. The activities of CK-MB and LDH were detected in the serum using homologous commercial kits (Elabscience and Beyotime) according to the manufacturer's instructions.

Echocardiography

The structure and function of the heart were assessed by echocardiography in rats anesthetized with isoflurane inhalation (2 %) using an ultrasound system (Philips EPIQ 7). The left ventricular end-diastolic diameter (LVIDd) and left ventricular end-systolic diameter (LVISd) were obtained using the M-mode analysis of a 2D short-axis view at the papillary muscle level, with the left ventricular ejection fraction (LVEF) and left ventricular fractional shortening (LVFS) being calculated automatically. Early diastolic mitral annular velocity (Ea) and late diastolic mitral annular velocity (Aa) were measured, and the ratio of Ea/Aa (E'/A' ratio) was calculated.

QUANTIFICATION AND STATISTICAL ANALYSIS

All data are presented as mean $\pm$ SEM. The GraphPad Prism (version 8; GraphPad Software, San Diego, CA, USA was used for statistical analyses. One-way analysis of variance (ANOVA) or Student's *t*-test was used for data analysis. A $p < 0.05$ was considered statistically significant.